Nano Research

Open Access

Research Article

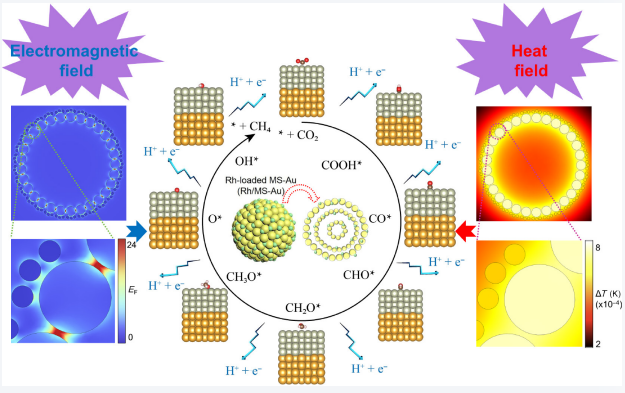
Multi-shell Au@Rh nanoantenna reactor with collective plasmonic excitation for photothermal CO_2 methanation

Hengrui Zhao[1,§], Jiazheng Wang[3,§], Yunhao Song[1], Dehui Sun[1] ✉, Qiang Zhang[2] ✉, Wei Lu[4] ✉, and Haiqing Wang[1] ✉

[1] *Shandong Key Laboratory of Functional Materials for Integrated Lithium Niobate Photonics, Institute of Advanced Interdisciplinary Research (IAIR), College of Chemistry and Chemical Engineering, University of Jinan, Jinan 250022, China*
[2] *College of Science, University of Shanghai for Science and Technology, Shanghai 200093, China*
[3] *School of Chemical Engineering, Shandong Institute of Petroleum and Chemical Technology, Dongying 257061, China*
[4] *College of Engineering, Ocean University of China, Qingdao 266100, China*
[§] *Hengrui Zhao and Jiazheng Wang contributed equally to this work.*

Cite this article: *Nano Research*, **2026**, *19*, 94908174. https://doi.org/10.26599/NR.2025.94908174

ABSTRACT: The photothermal pathway for converting carbon dioxide (CO_2) into hydrocarbons presents an effective and straightforward production for solar fuels. Nonetheless, the rational design of a robust solar-driven catalytic system for efficient CO_2 conversion remains a persistent challenge. In this work, we elaborately construct a multi-shell Au@Rh nanoantenna reactor for photothermal CO_2 methanation. The plasmonically active multi-shell Au structure serves as "antenna", and the catalytically active Rh nanoparticles function as "reactor". The reactor exhibits a superior CH_4 yield rate and nearly 100% selectivity, in comparison with the other Au structures (single-shell (SS) and nanoparticle) and the kinds of active sites (Ru, Ir, and Co). The well-arranged Au nanoparticles in multi-shell structure provide the collective plasmon-coupled excitation, leading to the strong localized surface plasmon resonance (LSPR) effect. Then, the antenna could convert the wide-spectrum solar energy to high surface temperature and enhanced electric field. The *in-situ* spectra and theoretical calculation indicate that the CO_2 methanation reaction in Au@Rh nanoantenna reactor follows the formyl pathway. The strong electron–proton coupling transfer ability of Au@Rh nanoantenna reactor contributes to the complex reaction pathway for CO_2 methanation. Especially, compared with Au catalyst, both the formation of COOH* intermediate and the key transformation from CO* to CHO* in Au@Rh nanoantenna reactor were promoted through the adequate supply of proton–electron pair and the strong interaction between Au and Rh sites. The ingenious design for nanoantenna reactor and the new findings in photothermal CO_2 methanation will inspire the development of mild hydrogenation for boosting CO_2-to-fuel conversion.



KEYWORDS: nanoantenna reactor, photothermal catalysis, CO_2 reduction, CO_2 methanation, collective plasmon excitation

1 Introduction

Solar-driven hydrogenation of CO_2 to produce value-added hydrocarbons is an entrancing strategy for building a sustainable, carbon-neutral economy [1, 2]. Among the various products of CO_2 reduction, the most reduced methane (CH_4) has the highest heating value and serves as a crucial feedstock for manufacturing various chemical products, such as aromatic hydrocarbons [3, 4]. Additionally, CH_4 as the primary component of natural gas, the existing infrastructure can seamlessly integrate with the photocatalytic CH_4 production [5, 6]. However, the bond breaking of C=O (750 kJ·mol^{-1}) in CO_2 is a dense-energy consuming process, which requires high utilization of solar power [7, 8]. The generation of CH_4 is both thermodynamically and kinetically unfavorable due to the prerequisite 8-electron and 8-proton coupling complicated transfer [9, 10]. The kinetically preferred carbon monoxide (CO) product is competing with the CO_2 methanation pathway through reverse water gas shift (RWGS) reaction [11, 12]. Taken together,

Received: August 20, 2025; **Revised:** September 29, 2025
Accepted: October 16, 2025

✉Address correspondence to Dehui Sun, ifc_sundh@ujn.edu.cn; Qiang Zhang, qiangzhang@usst.edu.cn; Wei Lu, 2024201@ouc.edu.cn; Haiqing Wang, ifc_wanghq@ujn.edu.cn

the weak light absorption, slow reaction kinetics, and competing CO-product pathway restrict the development of photocatalytic CO_2 methanation.

In recent years, the application of transition metal-based photocatalysts featuring localized surface plasmon resonance (LSPR) has gained significant attention for CO_2 reduction [13–15]. The transition metal-based LSPR nanostructures enable the transformation of incident light into elevated surface temperatures and intense electric fields. The surface plasmon resonance (SPR)-induced photo-electronic/thermal effect can be summarized as follows: (i) The hot electrons generated by the excitation of LSPR nanostructures can be directly injected into the conduction band of the semiconductor or the active metal sites to drive the chemical bond activation of inert CO_2 molecule [16–18]. (ii) The LSPR-induced electromagnetic field promotes the light absorption efficiency and enhances the adsorption and activation of intermediates [19, 20]. (iii) The LSPR nanostructures facilitate the absorption of light energy and the conversion of light energy into heat energy, reducing the activation energy barrier of the reaction [21–24]. However, the resonant responses of most transition metals are restricted to the ultraviolet (UV) and purple regions, which account for only 4% of the total solar spectrum (4% ultraviolet light, 43% visible light, and 53% infrared (IR) light), leading to low solar energy utilization efficiency. The rational design of a broad-spectrum solar-driven catalytic system for efficient CO_2 conversion remains a persistent challenge [25–27]. Some physical researches have exhibited that the LSPR effects were significantly enhanced at the neighboring spot of coupled nanostructures. The collective LSPR effect of plasmonic metal nanoparticles would be more favorable for the production of hot electrons as a way to meet the demand of 8-electron transfer for CH_4 generation [28]. However, most of current researches focus on isolated metal nanostructures [29–31]. It is still unknown what kind of extended architectures would be effective for the proximity of reactive sites to the electromagnetic fields of plasmonic metal, thus taking full advantage of the photo-to-heat and photo-to-electron transformations [32, 33].

Besides the effective light energy utilization and photothermal performance, the catalyst should also own sufficient ability for H_2 activation [34, 35]. The generated active H atoms serving as the key intermediates for CO_2 hydrogenation enable the hydrogenation reaction to occur at low onset temperatures [35–38]. Meanwhile, the amount of active H atoms provided by the catalyst has an obvious effect on the product selectivity. For example, a lower supply of active H atoms (2H*) favors the production of the kinetically preferred carbon monoxide (CO) [39–41]. When sufficient active H atoms (8H*) are provided, the CO can be further hydrogenated [42–45]. The rate and selectivity of CH_4 production will gradually increase. Therefore, the spatial arrangement and the chemical composition of the functional nanoparticles should be given primary consideration for designing catalyst towards effective photocatalytic CO_2 methanation.

Herein, we develop a multi-shell Au@Rh nanoantenna reactor (Rh/MS-Au) for wide-spectrum photothermal CO_2 methanation. This architecture integrates a plasmonic "antenna", the multi-shell Au structure, to harvest and convert wide-spectrum solar energy into intense heat and hot electrons, alongside a catalytic "reactor", Rh nanoparticles, to enable selective activation of CO_2 molecules. By bridging the gap between light absorption and catalytic reaction, the reactor overcomes the kinetic challenges of 8-electron/8-proton transfer and suppresses the competing RWGS pathway. Compared with the reference catalysts, the reactor exhibits a superior CH_4 yield rate and nearly 100% selectivity. Through *in-situ* spectroscopy and theoretical modeling, we unravel the formyl pathway enabled by the reactor, highlighting the critical role of proton–electron pair supply and metal–support interactions in promoting key reaction intermediates. This research endeavors to provide new insights into rational catalyst design for solar-driven CO_2 conversion.

2 Results and discussion

2.1 Synthesis and structure of Rh/MS-Au

The schematic preparation process of Rh/MS-Au is displayed in Fig. 1. Briefly, the multi-shell Au spheres (MS-Au) were prepared by a facile self-template strategy, typically including the synthesis of Au-melamine colloidal templates and the rapid *in-situ* reduction process. The single-shell Au spheres (Fig. S1 in the Electronic Supplementary Material (ESM)) and nanoparticles (Figs. S2 and S3 in the ESM) were prepared as reference substrates. After heating the mixture of multi-shell Au spheres and Rh salt in ethylene glycol, the metallic Rh nanoparticles were loaded into the porosity of multi-shell Au spheres. Thus, the bimetallic Au and Rh multi-shell structures, i.e., Rh/MS-Au, were prepared. The X-ray diffraction (XRD) pattern of the pristine MS-Au exhibits a well-crystallized metal Au phase (JCPDS 04-0784) (Fig. 2(a)). The diffraction peaks

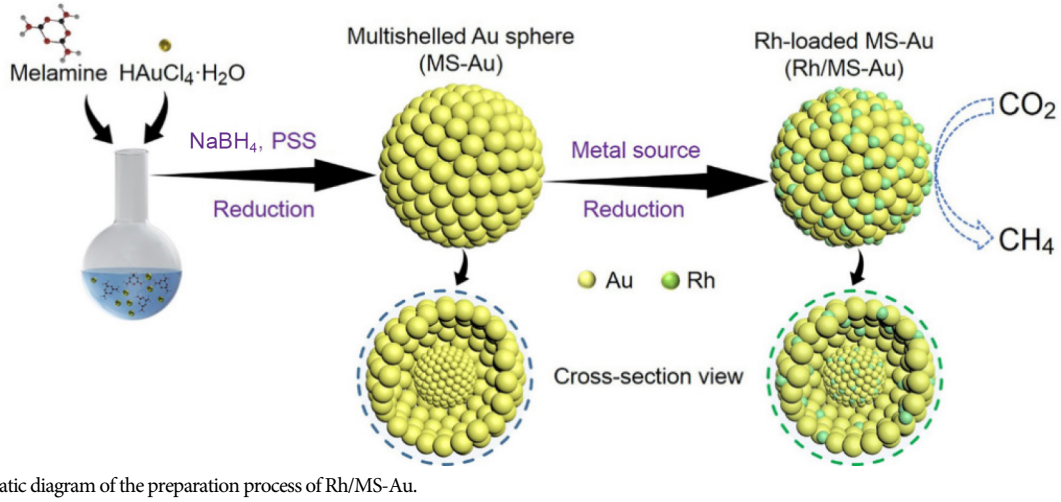


Figure 1 Schematic diagram of the preparation process of Rh/MS-Au.

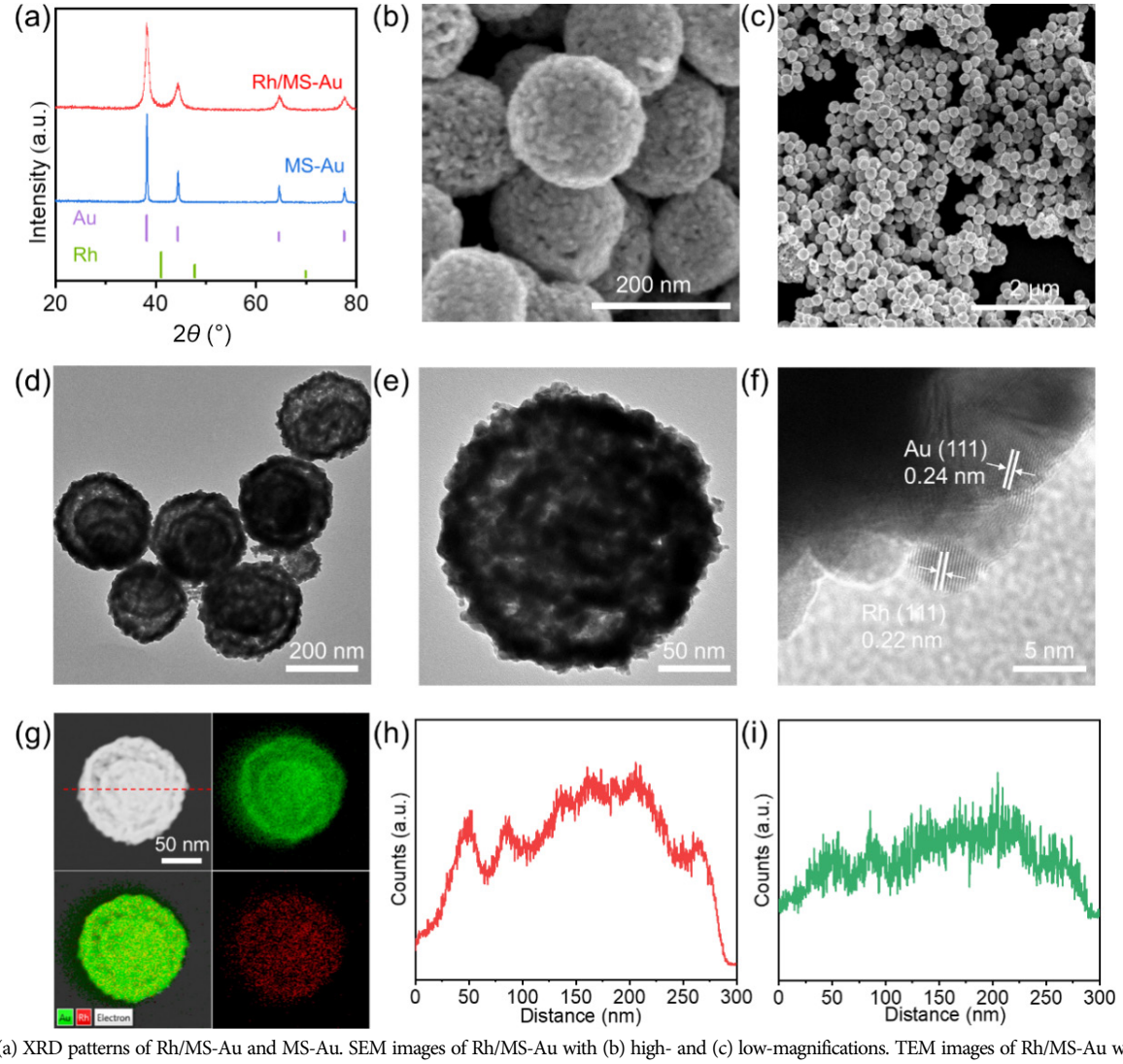


Figure 2 (a) XRD patterns of Rh/MS-Au and MS-Au. SEM images of Rh/MS-Au with (b) high- and (c) low-magnifications. TEM images of Rh/MS-Au with ((d) and (e)) low- and (f) high-magnifications. (g) HAADF-STEM image and the corresponding EDS elemental mapping images of Rh/MS-Au. EDX line scanning profiles of (h) Au and (i) Rh elements in Rh/MS-Au.

at 2θ = 38.2°, 44.4°, 64.6°, and 77.5° correspond to the Au (111), (200), (220), and (311) crystalline planes, respectively. After loading the metallic Rh nanoparticles, the XRD peaks belonging to Au remain almost the same positions, suggesting the well-preserved metal phase of Au in Rh/MS-Au. The diffraction peaks of Rh phase were not detected, implying the small size or the uniform dispersion of Rh nanoparticles on the Au surface in Rh/MS-Au. The structural and morphological features of the Rh/MS-Au catalysts were investigated using scanning electron microscopy (SEM) and high-resolution transmission electron microscopy (HR-TEM). As shown in Figs. 2(b) and 2(c), Rh/MS-Au displays highly rough surfaces and spherical shape with an outer diameter around 250 nm. The dynamic light scattering (DLS) test indicated that the particle size distribution is centered on 255 nm (Fig. S4 in the ESM). The low-magnification TEM image in Fig. 2(d) reveals that Rh/MS-Au possesses a clear porous triple-shell structure. Close observation indicates that Rh/MS-Au is assembled from nanoparticle structural units with sizes ranging from 5 to 10 nm (Fig. 2(e)). As illustrated in the HRTEM image (Fig. 2(f)), the lattice distances of 0.24 and 0.22 nm correspond to the (111) plane of metal Au and (111) plane of metal Rh, respectively. Ultrafine Rh nanoclusters with a diameter of 2–3 nm were decorated on the interstices of MS-Au. The high-angle annular dark field scanning transmission electron microscopy (HAADF-STEM) image of Rh/MS-Au in Fig. 2(g) displays an obvious contrast between the bright Au nanoparticle region and the dark fringe-positioned Rh region due to the difference in atomic number. The corresponding energy dispersive X-ray spectroscopy (EDS) mapping images illustrates the uniform distribution of Rh and Au elements in Rh/MS-Au. The energy dispersive X-ray (EDX) line scanning profile (Figs. 2(h) and 2(i)) across Rh/MS-Au illustrated sextuple signal peaks of Au and Rh, further verifying the hollow triple-shell structure and the loading of Rh onto the inner and outer Au shells. The Rh content in Rh/MS-Au is determined to be 0.54 wt.% by the inductively coupled plasma (ICP) test, which is also consistent with the 0.58 wt.% in Rh/SS-Au and 0.65 wt.% in Rh/Au. The nitrogen adsorption–desorption isotherm in Fig. S5 in the ESM indicates the specific surface area of 22.5 $m^2 \cdot g^{-1}$ and rich porosity for Rh/MS-Au. Taken together, Rh/MS-Au features the porous triple-shell structure and the aggregated nanoparticle structural units, demonstrating the favorable spatial arrangement for the collective plasmon excitation of Au and the interfacial mass transfer between Au and Rh.

The X-ray photoelectron spectroscopy (XPS) analysis in Fig. 3 was used to clarify the composition and the chemical valences of Rh/MS-Au. The full survey spectrum (Fig. S6 in the ESM) exhibits the chemical composition of Au and Rh in Rh/MS-Au, consistent with the above results of EDX elemental analysis. As shown in Fig. 3(a), the high-resolution XPS spectra of Au 4f show two typical peaks at ~ 84 eV of Au $4f_{7/2}$ and ~ 88 eV of Au $4f_{5/2}$, respectively [46, 47]. The XPS spectra of Rh 3d in Rh/MS-Au and elemental Rh (Figs. 3(b) and 3(c)) indicate the presence of $3d_{3/2}$ (about 307 and 309 eV) and $3d_{5/2}$ (about 312 and 314 eV) signals of Rh^0 and Rh^{3+} [48, 49]. The Rh species on SS-Au also shows a high proportion of Rh^{3+} in comparison with the Rh/Au (Fig. S7 in the ESM). The finding indicates high exposure of Rh species in the porous MS-Au and SS-Au. The surface oxidation of Rh should origin from the exposure to air. The interface interaction and charge transfer information were displayed by analyzing the chemical states of samples [50, 51]. Compared with MS-Au, the binding energy of Au 4f in Rh/MS-Au is up-shifted to 84.09 eV (by 0.32 eV), representing the electron transfer from Au to Rh. The Rh $3d_{3/2}$ binding energy shifts from 307.60 eV in elemental Rh to 307.34 eV in Rh/MS-Au by 0.26 eV. The blue shift of Rh 3d peaks indicates the electron transfer from Rh to Au, consistent with the Au 4f derived result. The observed electron transfer in Rh/MS-Au demonstrates the establishment of highly coupled Au–Rh interfaces, which could modulate the frontier orbital energies for effectively manipulating the adsorption, activation, and migration of reactive species towards photothermal CO_2 methanation.

The UV–visible (UV–Vis) spectra recorded from an aqueous suspension containing MS-Au, Rh/MS-Au, Rh/SS-Au, and Rh/Au are shown in Fig. 3(d). The reference Rh/Au exhibits weak light absorption capability from the UV region to the near infrared (NIR) region. The broad-range sunlight absorption properties were observed for MS-Au, Rh/MS-Au, and Rh/SS-Au. The absorption increase in the short-wavelength region from 350 to 500 nm should assign to the Rh LSPR [47, 52]. The interband transitions of Au also contribute to the signal intensity below 515 nm [28]. The difference in the light absorption capability of the above samples should be attributed to the collective plasmon excitation among the close mutual proximity of Au nanoparticles in single and multi-shell Au structures [28, 38]. The physical shell structure can promote the extra incident light reflections, which is also favorable for the light absorption [16, 18, 53]. In addition to the substrate Au structure, the metal/Au heterostructure usually exhibits the absorption enhancement in the visible light region through plasma resonance coupling, interfacial charge transfer, and defect-induced absorption, which are highly dependent on the structures of core–shell, alloy, and grain gap [54, 55–59]. The enhanced light absorption in Rh/MS-Au facilitates the increase of photogenerated carrier concentration and the enhancement of localized heating effects [60], thus accelerating surface reaction kinetics towards the reaction rate promotion. To further confirm the formation rate of photo-generated carrier under light illumination, the *j*–*t* transient patterns were recorded in Fig. 3(e). It can be observed that the on–off illumination cycles trigger fast current response for Rh/MS-Au and MS-Au samples. Obviously, the Rh/MS-Au sample with the Rh loading indicates an increase in the photocurrent, implying the enhanced ability to generate, separate, and transport photo-generated carrier under light excitation. Moreover, the photoluminescence (PL) spectra of Rh/MS-Au and MS-Au samples are given in Fig. 3(f). The signal intensity of the spectra is positively correlated with the recombination number of electrons and holes under photon emissions. It can be observed that the Rh loading significantly promotes the emission signal intensity of Rh/MS-Au in comparison with the reference MS-Au. The PL observations indicate that the Rh/MS-Au may own more active charges and more rapid transfer process to effectively participate in the photocatalytic reaction.

2.2 Performance for photothermal CO_2 methanation

The performance of photothermal CO_2 methanation was tested in a

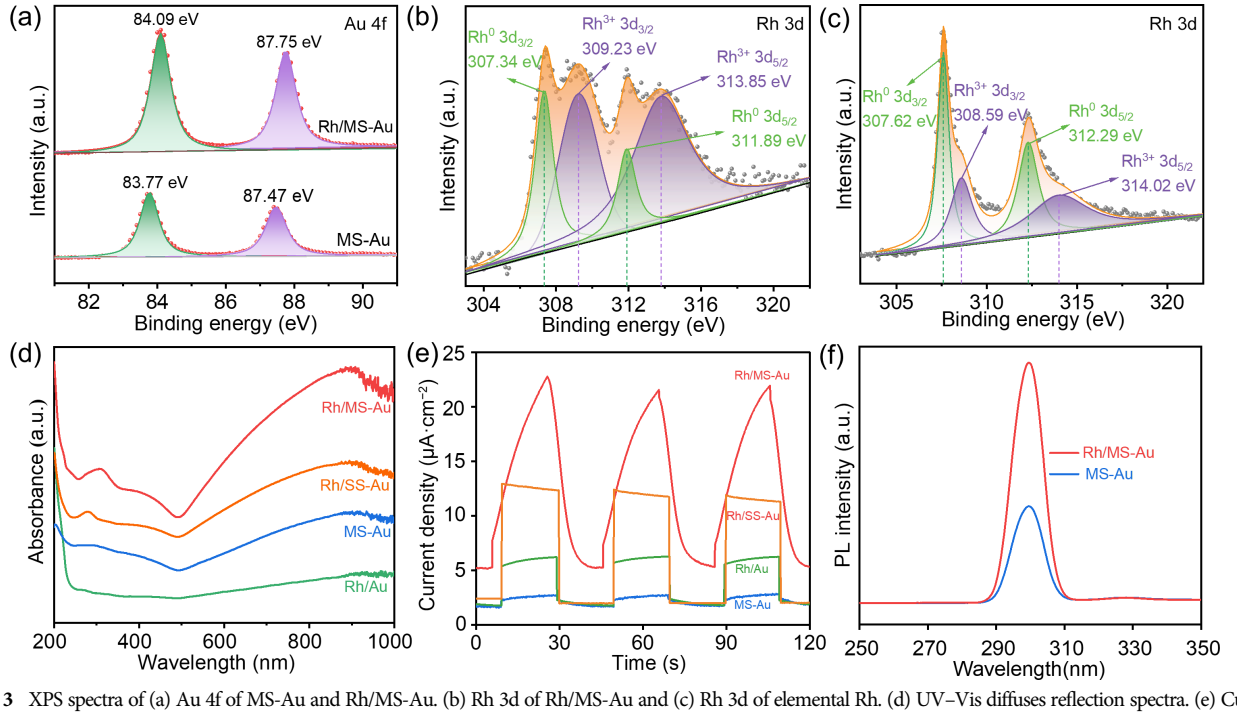


Figure 3 XPS spectra of (a) Au 4f of MS-Au and Rh/MS-Au. (b) Rh 3d of Rh/MS-Au and (c) Rh 3d of elemental Rh. (d) UV–Vis diffuses reflection spectra. (e) Current response under on-off illumination cycles. (f) PL emission spectra of MS-Au and Rh/MS-Au with a excitation wavelength of 300 nm.

sealed reaction chamber with CO_2 and H_2 as reactant gases. Firstly, we referred to the previous report [10], and the typical group VIII metals of Co, Rh, Ir, and Ru were used as loading metals to screen the active nanoparticles in a qualitative manner. The effects of loaded metal types on the reaction efficiency are evaluated in Fig. 4(a) and Fig. S8 in the ESM with MS-Au as substrate. The loaded Rh, Ir, and Ru metals exhibited 100% selectivity towards CH_4. The loaded Co catalyst prefers to generate CO product. The weak CO adsorption energy of pure MS-Au leads to difficulties in stabilizing CO. The limited H_2 activation capacity of MS-Au and Co/MS-Au results in a slow rate of H generation, which does not provide enough hydrogen species in time for CO hydrogenation. By contrast, the moderate CO adsorption energy and the strong H_2 activation capacity enable Rh, Ir, and Ru metals to stabilize the *CO species and to generate sufficient H source for CO_2 hydrogenation. The effects of the shell structure of substrate Au on the reaction efficiency are evaluated in Fig. 4(b). As mentioned before, MS/SS refers to multi-shell/single-shell Au sphere structure. Then the Rh/MS-Au, Rh/SS-Au, and Rh/Au catalysts were applied to screen out the proper substrate Au structure. As depicted in Fig. 4(b), the Rh loaded Au samples exhibited 100% selectivity towards the CH_4. The CH_4 evolution activity increased with the increase of the number of Au shells. Rh/MS-Au exhibited a CH_4 evolution rate of 8.05 $\mu mol \cdot g^{-1} \cdot h^{-1}$, which is considerably higher than 2.12 $\mu mol \cdot g^{-1} \cdot h^{-1}$ of Rh/SS-Au and 1.61 $\mu mol \cdot g^{-1} \cdot h^{-1}$ of Rh/Au samples. No CH_4 was detected for pure Au samples. The performance comparisons with other reports are provided in Table S1 in the ESM. The spatial arrangement in Rh/MS-Au with aggregated nanoparticle structural unit, adjacent triple shell, and abundant Au-Rh interface should favor the collective plasmon excitation of Au, the plasma resonance coupling of Au-Rh, and the interfacial mass transfer between Au and Rh, which synergistically leads to the catalytic performance enhancement. To further explore the activity origin of Rh/MS-Au, the experiments were then carried out with different waveband sunlight excitation (Fig. 4(c)). Although the prominent light-to-heat conversion under visible and IR light, the CH_4 generation rates measured under the irradiation of Vis and IR light were only 1.02 and 0.39 $\mu mol \cdot g^{-1} \cdot h^{-1}$, respectively, which occupied a low proportion in the CH_4 generation rate achieved by full spectrum. The UV light gave a production rate of 3.93 $\mu mol \cdot g^{-1} \cdot h^{-1}$. Strong electromagnetic fields and high concentrations of high-energy carriers generated by ultraviolet illumination should be responsible for the findings. The CH_4 productivity at the chamber temperature of 120 °C in the dark was further tested (Fig. 4(c)). The CH_4 production rate was only 1.52 $\mu mol \cdot g^{-1} \cdot h^{-1}$ without incident light, indicating that the chamber temperature alone cannot boost high-efficiency CO_2 hydrogenation. The above control tests confirm that the thermochemical pathway and photochemical pathway have a cooperative effect on the reaction rate of CO_2 methanation, typical of photothermal catalysis. In addition, Rh/MS-Au also exhibited high stability over an extended period of 20 h (Fig. 4(d)).

The average surface temperatures of the Rh/MS-Au, Rh/SS-Au, Rh/Au, and MS-Au catalysts were actually recorded *in-operando* by a FOTRIC 226 infrared camera, as exhibited in Figs. S9–S12 in the ESM, respectively. As shown in Fig. 5(a), the surface temperatures of the samples raised from room temperature to plateau temperature only in 300 s under the illumination of simulated 100 $mW \cdot cm^{-2}$ full spectra. Note that the bare MS-Au exhibited the lowest plateau temperature of 52.7 °C. The plateau temperatures of Rh/MS-Au, Rh/SS-Au, and Rh/Au samples are 122.7, 109.7, and 100.4 °C, respectively. The observation indicates that the Rh loading can significantly increase the plateau temperatures, implying a

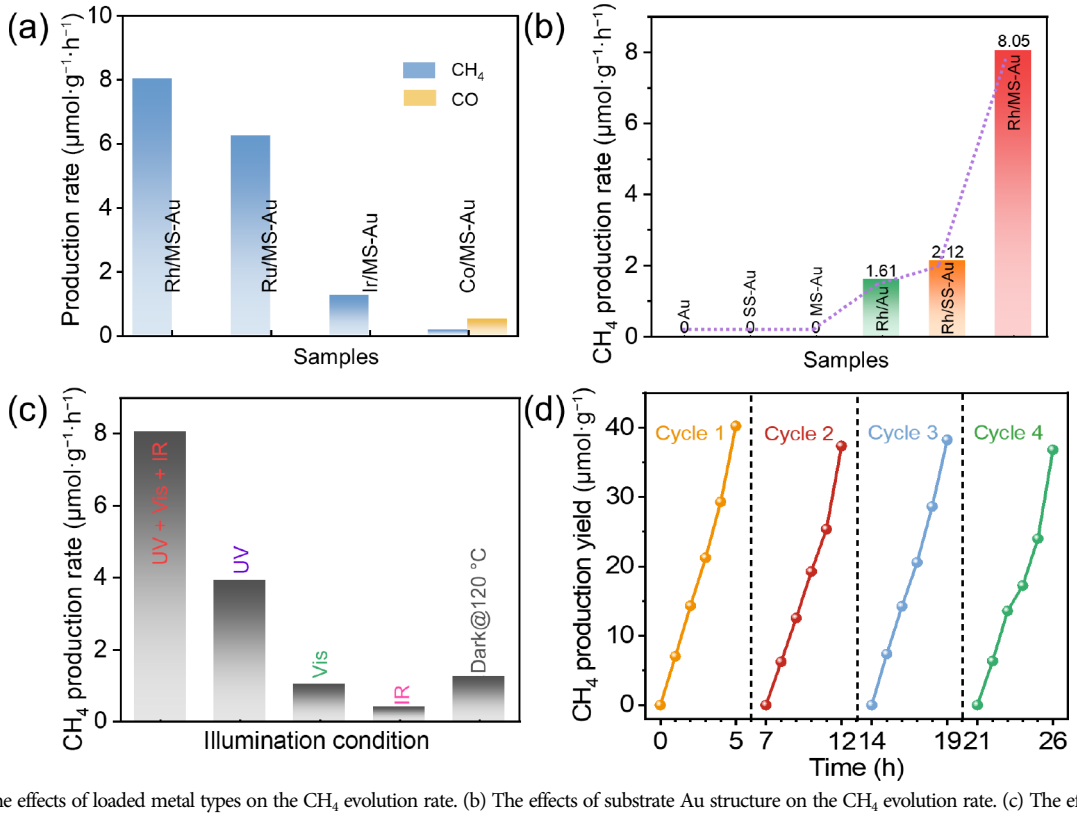


Figure 4 (a) The effects of loaded metal types on the CH_4 evolution rate. (b) The effects of substrate Au structure on the CH_4 evolution rate. (c) The effects of different waveband sunlight excitation on the CH_4 evolution rate. (d) Stability test of Rh/MS-Au.

higher capacity for converting light to heat. The plateau temperatures of samples with Rh loading show a positive correlation with the number of shell layers from Rh/Au to Rh/SS-Au, and to Rh/MS-Au. The effects of different waveband sunlight on the plateau temperature of Rh/MS-Au was studied. As given in Fig. 5(b), the visible waveband sunlight contributes a lot to the temperature rise for Rh/MS-Au. The plateau temperature under visible light illumination reaches up to about 100 °C, which is close to the top 122.7 °C under full spectrum illumination. Based on the distinct roles of driving forces in the reaction mechanism [4], the photothermal catalytic processes occurring in Rh/MS-Au can be classified as photo-driven thermocatalysis (PDTC), because the introduced sunlight acts as the sole source of heat. The actual multiple scattering of incident light within multi-shell Au structure may enhance light harvesting ability, thus promoting the light to heat conversion. The SPR coupling and the interfacial charge/energy transfer between Au and Rh should be responsible for the high plateau temperatures.

The simulations of optical heating and electromagnetic field are given in Fig. 6. Three geometric models were taken into consideration, in which the diameters of Au and Rh nanoparticles are set to be 10 and 3 nm, respectively. The first model is given in Figs. 6(a) and 6(e), featuring with randomly distributed Au nanoparticles (model I). As for the second model, the Au nanoparticles were placed in a circular arrangement to simulate the shell–layer Au structure, as shown in Figs. 6(b) and 6(f) (model II). The third model of circularly arranged Au-Rh structure in Figs. 6(c) and 6(g) was set by adding Rh nanoparticles in close proximity to each Au nanoparticle on the basis of the second structure with interparticle gap of 0.8 nm (model III).

Figures 6(a) and 6(e) show the electric field enhancement factor E_F ($E_F = E/E_0$, where E_0 is the electric field strength of incident light) and the temperature distribution around randomly distributed Au nanoparticles, respectively. The localized surface plasmon of individual nanoparticles only gives an enhancement factor of ~ 6 around each nanoparticle, and the scattered heat source leads to a meager increase of temperature. The enhancement factor and the temperature distribution of the simulated shell–layer Au structure are exhibited in Figs. 6(b) and 6(f). A series of plasmonic hot spots is clearly visible in the interparticle space of Au nanoparticles. In this case, the enhancement factor can reach up to ~ 22, which is significantly higher than that of randomly distributed Au nanoparticles. As a result, the individual particle in model II has witnessed a temperature increase of more than 15% in comparison with model I. Figures 6(c) and 6(g) show the enhancement factor and the temperature distribution of circularly arranged Au-Rh

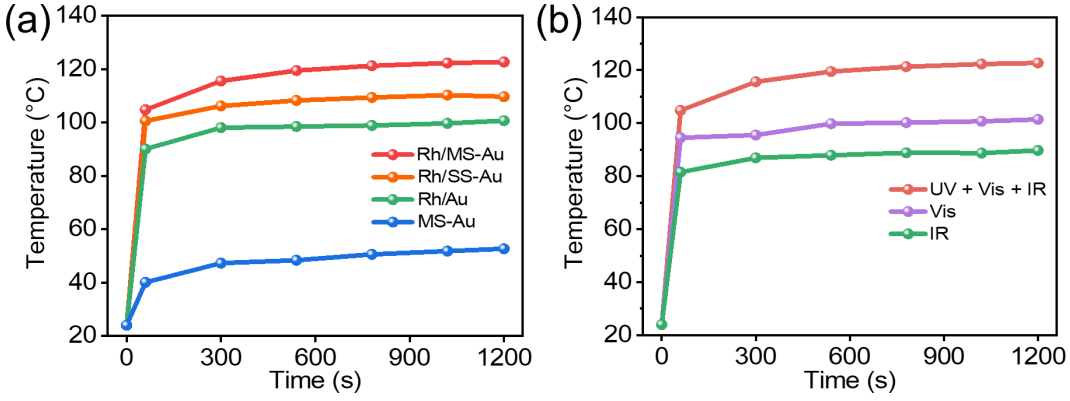


Figure 5 (a) Surface temperatures of Rh/MS-Au, Rh/SS-Au, MS-Au, and Rh/Au recorded by *in-operando* infrared camera. (b) Surface temperatures of Rh/MS-Au under different irradiation conditions.

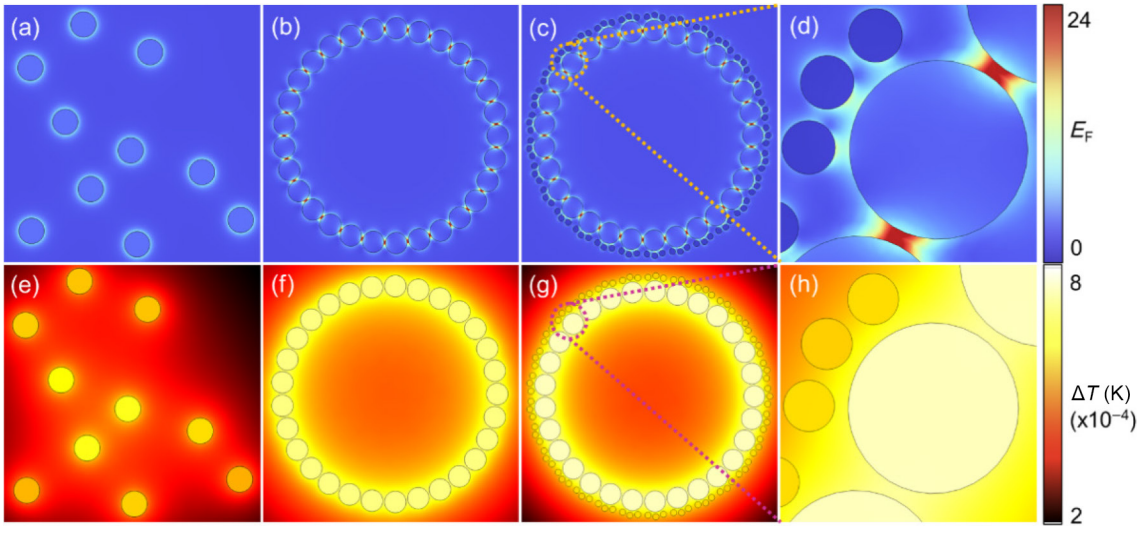


Figure 6 Electromagnetic field simulation for *E* field distribution around (a) randomly distributed Au nanoparticles, (b) circularly arranged Au structures, and (c) circularly arranged Au-Rh structures. (d) The local enlarged view of (c). Heat transfer simulation for temperature field around (e) randomly distributed Au nanoparticles, (f) circularly arranged Au structures, and (g) circularly arranged Au-Rh structures. (h) The local enlarged view of (g).

structures (model III), respectively. And the corresponding local enlarged views of Figs. 6(c) and 6(g) are provided in Figs. 6(d) and 6(h), respectively. The interfaces between Au and Rh nanoparticles in model III exhibit additional identified plasmonic hotspots on the basis of model II, though the enhancement factor is relatively smaller, approximately 10. Moreover, the existence of Rh nanoparticles can also serve as the additional heat source and contribute to the total temperature promotion of the Au-Rh composite system, leading to a temperature increase of about 13% in comparison with model II. The additional optical scattering coefficient and absorption coefficient on the corresponding model are calculated and exhibited in Figs. S13–S15 in the ESM. For all three models the scattering coefficient is minuscule compared to the absorption coefficient. Furthermore, the Au nanoparticles in models II and III show almost four time increase in absorption coefficient as well as red shift of LSPR adsorption peak because of plasmonic coupling. The LSPR of two and more adjacent Au nanoparticles is affected by plasmonic coupling. This plasmonic coupling generates enhanced electromagnetic field in the gap between nanoparticles, which is known as "hot-spots". This will increase the light absorption and scattering of nanoparticles and shift LSPR absorption peak toward longer wavelength [16, 34, 61, 62]. Also, an electromagnetic simulation on Au-Rh dimer was performed to clarify the LSPR effect between Rh and Au. As it can be seen in Fig. S16 in the ESM, the effect of Rh on the absorption of Au is rather small because of the small size of Rh nanoparticle, however, plasmonic coupling will increase the absorption coefficient on Rh significantly, indeed making them act as additional heat sources. Therefore, it can be reasonably predicted that the Au-Rh composite system will facilitate the charge transfer and reduce the kinetic obstacles for CO_2 photoreduction.

2.3 Insights into the photocatalytic mechanism of photothermal CO_2 methanation

Generally, the CO_2 methanation pathway can be divided into two main routes depending on the presence or absence of *CO intermediates [5]: (1) An oxygenate intermediate, i.e., *OCHO, instead of *CO, was generated by associating the adsorbed CO_2 and H_2 molecules. The target CH_4 product was formed after subsequent multiple hydrogenation steps. (2) The *CO intermediate derived from the dissociation of CO_2. The subsequent hydrogenation to generate CH_4 can be subdivided into three routes, i.e., carbene, formyl, and glyoxal pathways, as given in Fig. 7(a). To disclose the reaction pathway of CO_2 to CH_4, the intermediates generated during the CO_2 adsorption and conversion process on the surfaces of the Rh/MS-Au and the reference MS-Au were detected by *in-situ* diffuse reflectance infrared Fourier transform spectroscopy (DRIFTS). As shown in Figs. 7(b) and 7(c), the absorption band characteristics of the surface-adsorbed *CO_2 and the typical *CO, *COOH, *CHO, and *CH_3O intermediates were detected at about 1210, 2080, 1745, 1080, and 1106 cm^{-1}, respectively [5, 30, 63]. The signal intensities of the peaks increase as the reaction time prolongs from 8 to 64 min. According to the CO_2 methanation pathway presented in Fig. 7(c), no characteristic peaks correlative to carbene (such as *CH_2 and *CH_3) and glyoxal (C–C bond) pathways were detected. The signals of *CO, *COOH, *CHO, and *CH_3O intermediates are typical of formyl pathway [5]. Thus, the CO_2 methanation on the surface of Rh/MS-Au should follow the formyl pathway. In this case, the protonation of *CO to *CHO is recognized as the rate-determining step for CO_2 to CH_4. However, the *CO comes from the *COOH through the proton-electron transfer. The signals of *COOH and *CHO in Rh/MS-Au are significantly stronger than those in the reference MS-Au. The weak *CO signal in Rh/MS-Au indicates that *CO does not cause a large accumulation on the surface of Rh/MS-Au, thus avoiding the evolution of CO byproduct. It can also be speculated that the adsorption strength of *CO in Rh/MS-Au is moderate, and the proton–electron transfer is rapid in the conversion process of *COOH-to-*CO-to-*CHO in comparison with the reference MS-Au. As a result, the Rh/MS-Au exhibited high reaction activity and product selectivity in the formyl pathway towards CH_4.

To confirm aforementioned experimental results, the calculations about Gibbs free energy for photocatalytic CO_2 methanation reaction along the formyl pathway are described in Fig. 8(a). As revealed in Figs. 8(b) and 8(c), the formation of COOH*/CHO* intermediates is the potential-determining step. The reaction radical (CHO*) marked by the blue-dashed box is a key intermediate to determine the product selectivity, in which the brown (blue) line for Au@Rh (Au) refers to the favorable reaction

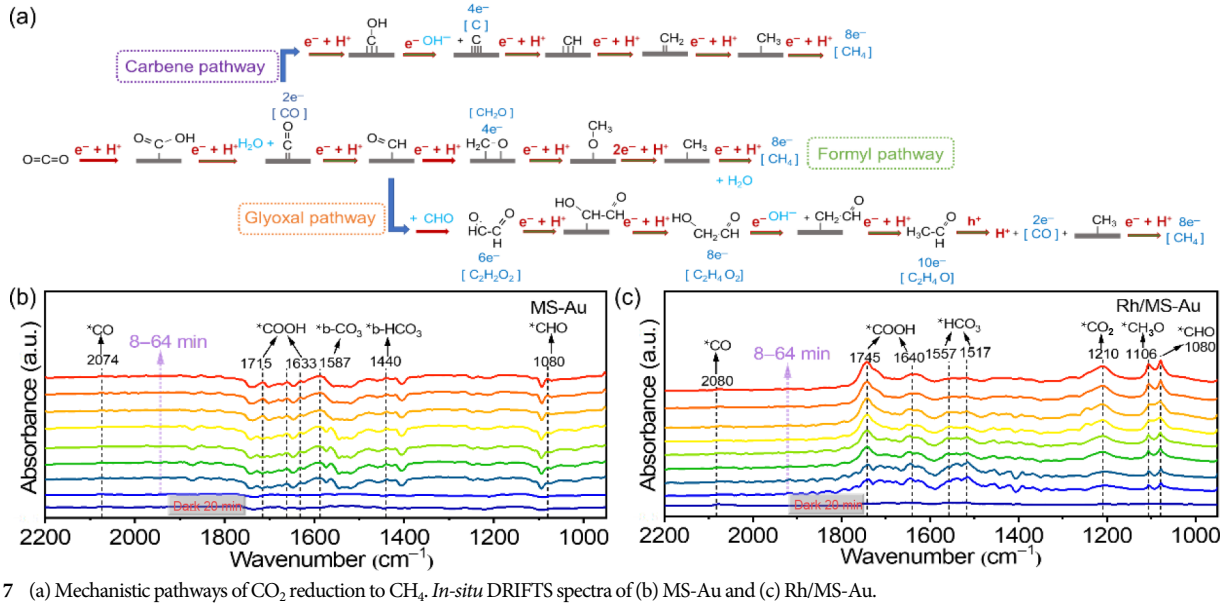


Figure 7 (a) Mechanistic pathways of CO_2 reduction to CH_4. *In-situ* DRIFTS spectra of (b) MS-Au and (c) Rh/MS-Au.

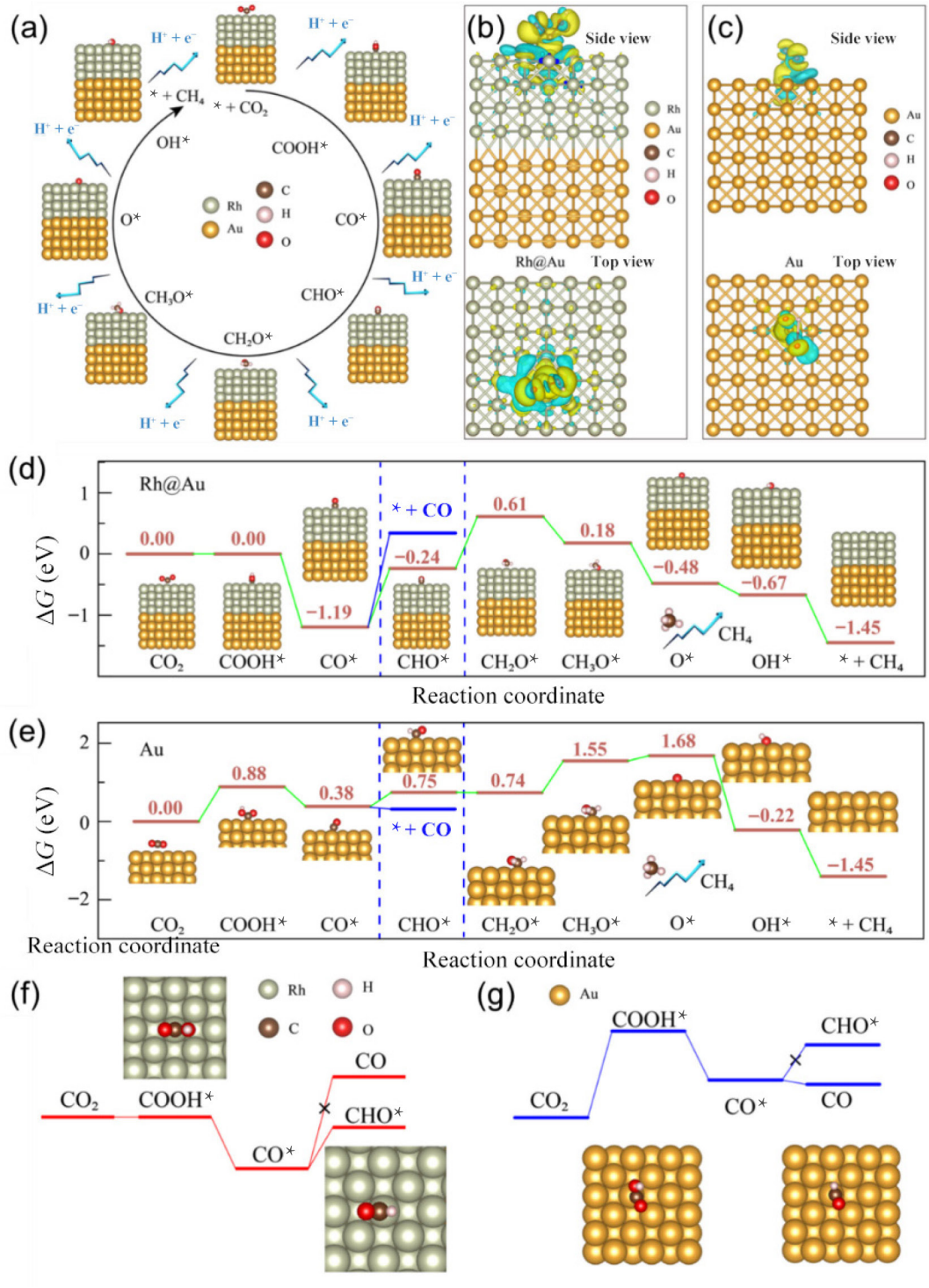


Figure 8 (a) A schematic diagram of reaction pathway for CO_2 photoreduction to CH_4. Free energy profiles of successive CO_2 protonation to CH_4 for (b) the Rh/Au and (c) pure Au catalysts. Differential charge density of CHO* intermediate for (d) the Rh/Au and (e) pure Au catalysts. The green/yellow isosurfaces represent the depletion/increase zone in the number of electrons, where the isosurfaces are set as 0.0035 eÅ^{-3}. Critical steps of photo-reduced CO_2-to-CH_4 for (f) the Rh/Au and (g) pure Au catalysts.

pathway. The Rh/Au and pure Au present different reaction selectivity. Compared with pure Au, the introduction of Rh atoms leads to a lower formation energy for COOH* on Rh/Au, which might be attributed to the redistribution of charges between COOH and slab. The differential charge density patterns are plotted in Figs. 8(d) and 8(e). The CHO* intermediates tend to bond more easily with the surface of Rh/Au than that of pure Au due to the enlarged hybridization between the d-orbital in Rh/Au and the p-orbital of CHO*. As a result, Rh/Au exhibits an obvious promotion for the adsorption of CHO*. For this scenario, the Gibbs free energy of the CHO* adsorption radical (ΔG_{CHO^*}) is significantly lower than the CO-desorption energy (ΔG_{*+CO}), as presented by the blue

dashed box in Fig. 6(b). The finding indicates that the formation of the CHO* adsorption species is a relatively easy process, whereas the process for CO molecule desorption needs to overcome a larger energy barrier. In other words, the Rh/Au slab is more beneficial for the CO*-protonation to generate CHO* than for the CO*-desorption, thus accounting for the high selectivity for the photoreduction of CO_2-to-CH_4. Contrastingly, ΔG_{*+CO} is lower than ΔG_{CHO*} for pure Au slab. As illustrated in Fig. 8(c), the CO*-desorption process is spontaneous, whereas the hydrogenation step of the CO* radical has to conquer a certain energy barrier. The CO* adsorption group could be easily desorbed from the surface of the pure Au catalyst to form the desorbed state. The adsorbed CO* intermediates can be further protonated by proton–electron pair to produce the main *CHO intermediate product on the surface of Rh/Au, leading to highly selective methanation reaction along the formyl pathway. Moreover, the desorption energy of the CH_4 molecule on the surface of Rh/Au is more negative than pure Au, suggesting the favorable CH_4 desorption step after the introduction of Rh atoms. This is likely attributed to the generation of a new C–H bond by another proton–electron pair attacking CH_3O. The resultant C coordination saturation makes the CH_3 component to be easily desorbed from the surface of Rh/Au. The remaining and unsaturated O atoms in CH_3O can be firmly adsorbed on the surface atoms due to the intense d-p hybridization. As for the CH_3O* adsorption species on pure Au slab, the stronger hybridization between the O p and Rh d orbitals weakens C–O bond in the CH_3O* group, which facilitates the breakage between C–O and thus reduces the desorption potential barrier of CH_4.

Taken together, as illustrated in Figs. 8(f) and 8(g), Rh/Au can promote the photocatalytic CO_2 methanation reaction along the formyl pathway. Firstly, Rh/Au can provide more active sites to efficiently stabilize the COOH* precursor. Secondly, Rh/Au possesses an enhanced bonding with the CHO* adsorption species, favoring the formyl pathway towards CH_4. Thirdly, the strong d-p hybridization between Rh/Au and the O atoms of CH_3O* boosts the breakage of C–O bond in CH_3O*, thereby reducing the CH_4-desorption energy barrier. All these merits enable the Rh/Au photocatalyst to convert CO_2 to CH_4 with high selectivity and activity.

3 Conclusions

In this study, a multi-shell Au@Rh nanoantenna reactor (Rh/MS-Au) was developed for efficient photothermal CO_2 methanation. The hierarchical architecture of Au "antenna" leverages collective plasmonic coupling to broaden solar absorption and enhance light-to-heat/electron conversion. The Rh nanoparticles facilitate H_2 activation and stabilize critical intermediates. Rh/MS-Au exhibited a superior CH_4 yield rate of 8.05 $\mu mol \cdot g^{-1} \cdot h^{-1}$ with nearly 100% selectivity, outperforming single-shell Au and Au nanoparticle counterparts. *In-situ* DRIFTS and density functional theory (DFT) calculations revealed that the reaction occurred on the surface of Rh/MS-Au followed a formyl pathway. The strong proton–electron pair supply in Rh/MS-Au was beneficial for stabilizing key intermediates and reducing the energy barrier for CO hydrogenation to CHO. This work highlights the critical role of spatial arrangement and bimetallic synergy in overcoming kinetic challenges in CO_2 methanation, providing a novel strategy for designing broad-spectrum photothermal catalysts for sustainable CO_2-to-fuel conversion under mild conditions.

Electronic Supplementary Material: Supporting material (experimental procedure, theoretical simulation, SEM, TEM, photothermal test, and so on) is available in the online version of this article at https://doi.org/10.26599/NR.2025.94908174.

Data availability

All data needed to support the conclusions in the paper are presented in the manuscript and the Electronic Supplementary Material. Additional data related to this paper may be requested from the corresponding author upon request.

Acknowledgements

This work was supported by the National Natural Science Foundation of China (Nos. 92477134 and 52572007), the National Key Research and Development Program of China (No. 2023YFB3507700), the Taishan Scholar Project of Shandong Province (No. tsqn202408205), and Provincial Natural Science Foundation of Shandong (No. ZR2023ME014).

Declaration of competing interest

All the contributing authors report no conflict of interests in this work.

Author contribution statement

H. R. Z. and Y. H. S. conducted the experiment. J. Z. W. performed the field simulation. H. Q. W. designed the project and conducted the experiments. Q. Z. conducted the theoretical analysis. W. L. and D. H. S. helped optimize the experiment design and further polished the manuscript.

Use of AI statement

None.

References

[1] Zhou, L. N.; Martirez, J. M. P.; Finzel, J.; Zhang, C.; Swearer, D. F.; Tian, S.; Robatjazi, H.; Lou, M. H.; Dong, L. L.; Henderson, L. et al. Light-driven methane dry reforming with single atomic site antenna-reactor plasmonic photocatalysts. *Nat. Energy* **2020**, *5*, 61–70.

[2] Zhang, X.; Li, X. Q.; Zhang, D.; Su, N. Q.; Yang, W. T.; Everitt, H. O.; Liu, J. Product selectivity in plasmonic photocatalysis for carbon dioxide hydrogenation. *Nat. Commun.* **2017**, *8*, 14542.

[3] Song, C. Q.; Wang, Z. H.; Yin, Z.; Xiao, D. Q.; Ma, D. Principles and applications of photothermal catalysis. *Chem Catal.* **2022**, *2*, 52–83.

[4] Zhou, J.; Liu, H.; Wang, H. Q. Photothermal catalysis for CO_2 conversion. *Chin. Chem. Lett.* **2023**, *34*, 107420.

[5] Wang, Y. O.; Chen, E. Q.; Tang, J. W. Insight on reaction pathways of photocatalytic CO_2 conversion. *ACS Catal.* **2022**, *12*, 7300–7316.

[6] Fu, G.; Jiang, M. H.; Liu, J.; Zhang, K. Q.; Hu, Y.; Xiong, Y.; Tao, A. Y.; Tie, Z.; Jin, Z. Rh/Al nanoantenna photothermal catalyst for wide-spectrum solar-driven CO_2 methanation with nearly 100% selectivity. *Nano Lett.* **2021**, *21*, 8824–8830.

[7] Li, J. J.; Abbas, S. U.; Wang, H. Q.; Zhang, Z. C.; Hu, W. P. Recent advances in interface engineering for electrocatalytic CO_2 reduction reaction. *Nano-Micro Lett.* **2021**, *13*, 216.

[8] Wang, H. Q. Nanostructure@metal-organic frameworks (MOFs) for catalytic carbon dioxide (CO_2) conversion in photocatalysis, electrocatalysis, and thermal catalysis. *Nano Res.* **2022**, *15*, 2834–2854.

[9] Li, W.; Wang, E. Y.; Wang, H. Q.; Yang, Y.; Hu, S. X.; Liu, H. Construction of S-scheme heterostructure via anion and cation vacancy mediated electrostatically driven self-assembly in $Cd_{1-x}S$-CdS_{1-x} for robust photocatalytic CO_2 reduction. *Nano Energy* **2025**, *142*, 111235.

[10] Meng, X. G.; Wang, T.; Liu, L. Q.; Ouyang, S. X.; Li, P.; Hu, H. L.; Kako, T.; Iwai, H.; Tanaka, A.; Ye, J. H. Photothermal conversion of CO_2 into CH_4 with H_2 over group VIII nanocatalysts: An alternative approach for solar fuel production. *Angew. Chem., Int. Ed.* **2014**, *53*, 11478–11482.

[11] Yu, J. B.; Muhetaer, A.; Gao, X. W.; Zhang, Z. Z.; Yang, Y. Y.; Li, Q.; Chen, L. X.; Liu, H. C.; Xu, D. S. Highly active hydrogen-rich photothermal reverse water gas shift reaction on Ni/$LaInO_3$ perovskite catalysts with near-unity selectivity. *Angew. Chem., Int. Ed.* **2023**, *62*, e202303135.

[12] Robatjazi, H.; Zhao, H. Q.; Swearer, D. F.; Hogan, N. J.; Zhou, L. N.; Alabastri, A.; McClain, M. J.; Nordlander, P.; Halas, N. J. Plasmon-induced selective carbon dioxide conversion on earth-abundant aluminum-cuprous oxide antenna-reactor nanoparticles. *Nat. Commun.* **2017**, *8*, 27.

[13] Luo, S. Q.; Ren, X. H.; Lin, H. W.; Song, H.; Ye, J. H. Plasmonic photothermal catalysis for solar-to-fuel conversion: Current status and prospects. *Chem. Sci.* **2021**, *12*, 5701–5719.

[14] Ge, H.; Kuwahara, Y.; Kusu, K.; Bian, Z. F.; Yamashita, H. Ru/H_xMoO_{3-y} with plasmonic effect for boosting photothermal catalytic CO_2 methanation. *Appl. Catal. B: Environ.* **2022**, *317*, 121734.

[15] Jiang, D.; Yuan, H. F.; Liu, Z.; Chen, Y. K.; Li, Y. Y.; Zhang, X. L.; Xue, G. B.; Liu, H.; Liu, X. Y.; Zhao, L. L. et al. Defect-anchored single-atom-layer Pt clusters on TiO_{2-x}/Ti for efficient hydrogen evolution via photothermal reforming plastics. *Appl. Catal. B: Environ.* **2023**, *339*, 123081.

[16] Ninakanti, R.; Borah, R.; Craig, T.; Ciocarlan, R. G.; Cool, P.; Bals, S.; Verbruggen, S. W. Au@TiO_2 core–shell nanoparticles with nanometer-controlled shell thickness for balancing stability and field enhancement in plasmon-enhanced photocatalysis. *ACS Nano* **2024**, *18*, 33430–33440.

[17] Wan, Y. T.; Fang, F.; Sun, R. X.; Zhang, J.; Chang, K. Metal oxide semiconductors for photothermal catalytic CO_2 hydrogenation reactions: Recent progress and perspectives. *Acta Phys. Chim. Sin.* **2023**, *39*, 2212042.

[18] Chen, Y. A.; Nakayasu, Y.; Lin, Y. C.; Kao, J. C.; Hsiao, K. C.; Le, Q. T.; Chang, K. D.; Wu, M. C.; Chou, J. P.; Pao, C. W. et al. Double-hollow Au@CdS yolk@shell nanostructures as superior plasmonic photocatalysts for solar hydrogen production. *Adv. Funct. Mater.* **2024**, *34*, 2402392.

[19] Borah, R.; Verbruggen, S. W. Nanoscale energy balance of a plasmonic antenna–reactor catalyst for light-driven reactions: The role of hot-carriers vs the photothermal effect. *ACS Nano* **2025**, *19*, 19962–19976.

[20] Yang, Y.; Yang, Y.; Chen, S. M.; Lu, Q. C.; Song, L.; Wei, Y.; Wang, X. Atomic-level molybdenum oxide nanorings with full-spectrum absorption and photoresponsive properties. *Nat. Commun.* **2017**, *8*, 1559.

[21] Chu, M. Y.; Yan, P. L.; Zhou, Y. X.; Lou, X. X.; Li, C. R.; Cao, M. H.; He, L.; Zhang, Q.; Chen, J. X. Plasmonic copper-ruthenium superstructure for efficient photothermal conversion and plastic recycling. *Adv. Funct. Mater.* **2025**, *35*, 2417644.

[22] Lu, Q. C.; Wang, X. Recent progress of sub-nanometric materials in photothermal energy conversion. *Adv. Sci.* **2022**, *9*, 2104225.

[23] Zhang, H. B.; Wang, C. J. Photothermal synergistic catalysis and associated kinetics. *China Powder Sci. Technol.* **2025**, *31*, 11–21.

[24] Xu, B.; Zhang, W. J.; Zhou, Z. H.; Lu, X. Q.; Li, J.; Pan, G. L.; Lou, Y. Research progress on thermoelectric metalorganic frameworks and covalent organic frameworks materials. *China Powder Sci. Technol.* **2025**, *31*, 61–73.

[25] Li, M. Q.; Han, Z. Q.; Kong, J.; Hu, Q. Y.; Liu, W. X.; Xu, J. Q.; Yan, W. S.; Hu, J.; Zhu, J. F.; Pan, Y. et al. Infrared photothermal catalytic reduction of atmospheric CO_2 into CO with 100% selectivity via dual-plasmon resonance conductor. *Adv. Mater.* **2025**, *37*, 2503021.

[26] Zhang, S. M.; Shi, Y. A.; He, T.; Ni, B.; Li, C. Z.; Wang, X. Ultrathin tungsten bronze nanowires with efficient photo-to-thermal conversion behavior. *Chem. Mater.* **2018**, *30*, 8727–8731.

[27] Pan, Q.; Li, J.; Yan, L. G. Research progress of photothermal material-wood evaporators for solar-driven interfacial evaporation. *China Powder Sci. Technol.* **2024**, *30*, 90–102.

[28] Yu, G. Y.; Qian, J.; Zhang, P.; Zhang, B.; Zhang, W. X.; Yan, W. F.; Liu, G. Collective excitation of plasmon-coupled Au-nanochain boosts photocatalytic hydrogen evolution of semiconductor. *Nat. Commun.* **2019**, *10*, 4912.

[29] Wang, H. M.; Shang, B.; Choi, C.; Jeon, S.; Gao, Y. Z.; Wang, T.; Harmon, N. J.; Liu, M. X.; Stach, E. A.; Wang, H. L. Enhanced methanol production from photothermal CO_2 reduction via multilevel interface design. *Nano Res.* **2025**, *18*, 94907160.

[30] Zhu, C. Y.; Huang, H. M.; Hu, H. L.; Fang, J. J.; Mao, J. J. Modulation of oxygen vacancies and hot electrons promotes highly efficient CO_2 photoreduction towards C_2H_6. *Nano Res.* **2025**, *18*, 94907275.

[31] Talib, S. H.; Jiang, X. L.; Feng, S. X.; Zhao, M. D.; Yu, Q. Theoretical catalytic performance of single-atom catalysts $M_1/PW_{12}O_{40}$ for alkyne hydrogenation materials. *Nano Res. Energy* **2024**, *3*, e9120128.

[32] Li, S. J.; Yang, J. L.; Ruan, X. W.; Cui, X. Q.; Ravi, S. K. Plasmonic nanomaterials in photothermal catalysis and artificial photosynthesis: Hot electron dynamics, design challenges, and future prospects. *Adv. Funct. Mater.*, in press, https://doi.org/10.1002/adfm.202503186.

[33] Zhang, S. M.; Lu, Q. C.; Yu, B.; Cheng, X. J.; Zhuang, J.; Wang, X. Polyoxometalates facilitating synthesis of subnanometer nanowires. *Adv. Funct. Mater.* **2021**, *31*, 2100703.

[34] Yang, J. L.; He, Y. L.; Ren, H.; Zhong, H. L.; Lin, J. S.; Yang, W. M.; Li, M. D.; Yang, Z. L.; Zhang, H.; Tian, Z. Q. et al. Boosting photocatalytic hydrogen evolution reaction using dual plasmonic antennas. *ACS Catal.* **2021**, *11*, 5047–5053.

[35] Hong, J. N.; Xu, C. Y.; Liu, Y.; Li, C. Q.; Wang, M. L.; Zhang, Y. W. Decoding the interfacial competition between hydrogen evolution and CO_2 reduction via edge-active-site modulation in photothermal catalysis. *Acta Phys. Chim. Sin.* **2025**, *41*, 100099.

[36] Ji, G. R.; Ji, L.; Wu, S. W.; Meng, L. X.; Jia, Y. T.; Liu, Z. N.; Dong, S. H.; Tian, J.; Li, Y. Z. *In-situ* exsolved ultrafine Ni nanoparticles from $CeZrNiO_2$ solid solution for efficient photothermal catalytic CO_2 reduction by CH_4. *Adv. Powder Mater.* **2024**, *3*, 100188.

[37] Li, L.; Dai, X. Y.; Lu, M. C.; Guo, C. F.; Wabaidur, S. M.; Wu, X. L.; Lou, Z. R.; Zhong, Y. J.; Hu, Y. Electron-enriched single-Pd-sites on g-C_3N_4 nanosheets achieved by *in-situ* anchoring twinned Pd nanoparticles for efficient CO_2 photoreduction. *Adv. Powder Mater.* **2024**, *3*, 100170.

[38] Zhong, Q. X.; Feng, J.; Jiang, B.; Fan, Y. L.; Zhang, Q.; Chen, J. X.; Yin, Y. D. Strain-modulated seeded growth of highly branched black Au superparticles for efficient photothermal conversion. *J. Am. Chem. Soc.* **2021**, *143*, 20513–20523.

[39] Sun, C. Y.; Li, W.; Wang, K.; Zhou, W. J.; Wang, H. Q. Polyoxometalates-derived nanostructures for electrocatalysis application. *Rare Met.* **2024**, *43*, 1845–1866.

[40] Xie, Z. H.; Hwang, S.; Chen, J. G. Reduction-induced metal/oxide interfacial sites for selective CO_2 hydrogenation. *SmartMat* **2023**, *4*, e1201.

[41] Qiao, F. Photoelectrocatalytic hydrogen production: Hydrogen production principle, performance optimization strategy, application and prospect. *Nano Res. Energy* **2025**, *4*, e9120132.

[42] Dai, F. X.; Zhang, M. M.; Han, J. S.; Li, Z. J.; Feng, S. H.; Xing, J.;

Wang, L. Bifunctional core–shell co-catalyst for boosting photocatalytic CO_2 reduction to CH_4. *Nano Res.* **2024**, *17*, 1259–1266.
[43] Song, Y. H.; Zhao, H. R.; Lu, W.; Wang, H. Q. Unlocking hydrogen transfer pathway in electrocatalytic CO_2 reduction: Paving the way for precise selectivity control. *Nano Res.* **2025**, *18*, 94907384.
[44] Qiu, N.; Lu, W.; Wang, H. Q. Manipulating local CO_2/H_2O ratio in electrocatalytic CO_2 reduction toward multi-carbon product. *Rare Met.* **2025**, *44*, 60–80.
[45] Song, Y. H.; Zhao, H. R.; Lu, W.; Wang, H. Q. Visualizing atom-scale surface restructuring of Cu-based electrocatalyst in electrocatalytic CO_2 reduction toward multicarbon product. *Rare Met.* **2025**, *44*, 4309–4311.
[46] Sun, M. Q.; Fu, X. Q.; Chen, K. X.; Wang, H. Dual-plasmonic gold@copper sulfide core–shell nanoparticles: Phase-selective synthesis and multimodal photothermal and photocatalytic behaviors. *ACS Appl. Mater. Interfaces* **2020**, *12*, 46146–46161.
[47] de Souza Rodrigues, M. P.; Dourado, A. H. B.; Cutolo, L. D. O.; Parreira, L. S.; Alves, T. V.; Slater, T. J. A.; Haigh, S. J.; Camargo, P. H. C.; Cordoba de Torresi, S. I. Gold-rhodium nanoflowers for the plasmon-enhanced hydrogen evolution reaction under visible light. *ACS Catal.* **2021**, *11*, 13543–13555.
[48] Wang, C. Y.; Schechter, A.; Feng, L. G. Iridium-based catalysts for oxygen evolution reaction in acidic media: Mechanism, catalytic promotion effects and recent progress. *Nano Res. Energy* **2023**, *2*, e9120056.
[49] Mu, Y. L.; Chu, F. L.; Wang, B. L.; Huang, T. Z.; Ding, Z. Y.; Ma, D. L.; Liu, F.; Liu, H.; Wang, H. Q. Manipulating crystallographic growth orientation by cation-enhanced gel-polymer electrolytes toward reversible low-temperature zinc-ion batteries. *InfoMat* **2024**, *6*, e12611.
[50] Li, L.; Zhang, Z. C. Ultrasmall high-entropy alloy nanoparticles with 1 nm size by continuous-flow reactor. *SmartMat* **2024**, *5*, e1239.
[51] Liu, J. W.; Lee, C.; Hu, Y.; Liang, Z. S.; Ji, R.; Soo, X. Y. D.; Zhu, Q.; Yan, Q. Y. Recent progress in intermetallic nanocrystals for electrocatalysis: From binary to ternary to high-entropy intermetallics. *SmartMat* **2023**, *4*, e1210.
[52] Cui, J.; Zhang, S. X.; Xu, X. L.; Ren, K.; Dong, M. Z.; Nie, Z. K.; Xu, Y.; Dai, X. H.; Xu, P.; Sun, S. et al. Recent advances of nanomaterials in imaging liver fibrosis. *BMEMat* **2025**, *3*, e12123.
[53] Li, H.; Cheng, C. K.; Yang, Z. J.; Wei, J. J. Encapsulated CdSe/CdS nanorods in double-shelled porous nanocomposites for efficient photocatalytic CO_2 reduction. *Nat. Commun.* **2022**, *13*, 6466.
[54] Jiang, W. B.; Low, B. Q. L.; Long, R.; Low, J.; Loh, H.; Tang, K. Y.; Chai, C. H. T.; Zhu, H. J.; Zhu, H.; Li, Z. B. et al. Active site engineering on plasmonic nanostructures for efficient photocatalysis. *ACS Nano* **2023**, *17*, 4193–4229.
[55] Li, Z.; Gong, J. C.; Lu, S.; Li, X. J.; Gu, X. B.; Xu, J.; Khan, J. U.; Jin, D. Y.; Chen, X. Y. Photothermal lanthanide nanomaterials: From fundamentals to theranostic applications. *BMEMat* **2024**, *2*, e12088.
[56] Wei, P.; Wang, H. Y.; Yang, M.; Wang, J. Y.; Wang, D. Relocatable hollow multishelled structure-based membrane enables dendrite-free lithium deposition for ultrastable lithium metal batteries. *Adv. Energy Mater.* **2024**, *14*, 2400108.
[57] Wang, J. Y.; Wan, J. W.; Yang, N. L.; Li, Q.; Wang, D. Hollow multishell structures exercise temporal-spatial ordering and dynamic smart behaviour. *Nat. Rev. Chem.* **2020**, *4*, 159–168.
[58] Zhang, H.; Zhang, S. C.; Guo, B. Y.; Yu, L. J.; Ma, L. L.; Hou, B. X.; Liu, H. Y.; Zhang, S. H.; Wang, J. Y.; Song, J. J. et al. MoS_2 hollow multishelled nanospheres doped Fe single atoms capable of fast phase transformation for fast-charging Na-ion batteries. *Angew. Chem., Int. Ed.* **2024**, *63*, e202400285.
[59] Zhang, X.; Bi, R. Y.; Wang, J. Y.; Zheng, M.; Wang, J.; Yu, R. B.; Wang, D. Delicate co-control of shell structure and sulfur vacancies in interlayer-expanded tungsten disulfide hollow sphere for fast and stable sodium storage. *Adv. Mater.* **2023**, *35*, 2209354.
[60] Baffou, G.; Bordacchini, I.; Baldi, A.; Quidant, R. Simple experimental procedures to distinguish photothermal from hot-carrier processes in plasmonics. *Light: Sci. Appl.* **2020**, *9*, 108.
[61] Jain, P. K.; El-Sayed, M. A. Plasmonic coupling in noble metal nanostructures. *Chem. Phys. Lett.* **2010**, *487*, 153–164.
[62] Jain, P. K.; Lee, K. S.; El-Sayed, I. H.; El-Sayed, M. A. Calculated absorption and scattering properties of gold nanoparticles of different size, shape, and composition: Applications in biological imaging and biomedicine. *J. Phys. Chem. B* **2006**, *110*, 7238–7248.
[63] Cao, Y. H.; Guo, L.; Dan, M.; Doronkin, D. E.; Han, C. Q.; Rao, Z. Q.; Liu, Y.; Meng, J.; Huang, Z. A.; Zheng, K. B. et al. Modulating electron density of vacancy site by single Au atom for effective CO_2 photoreduction. *Nat. Commun.* **2021**, *12*, 1675.

This is an open access article under the terms of the Creative Commons Attribution 4.0 International License (CC BY 4.0, https://creativecommons.org/licenses/by/4.0/).

© The Author(s) 2026. Published by Tsinghua University Press.